![Helmholtz-Zentrum Geesthacht — Zentrum für Material- und Küstenforschung]

Final Draft
of the original manuscript:

Mg-Ca binary alloys as anodes for primary Mg-air batteries

Min Deng[a,*], Daniel Höche[a, b], Sviatlana V. Lamaka[a], Darya Snihirova[a], Mikhail L. Zheludkevich[a, c]

[a] MagIC—Magnesium Innovation Centre, Helmholtz-Zentrum Geesthacht (HZG), 21502 Geesthacht, Germany

[b] Computational Material Design, Faculty of Mechanical Engineering, Helmut-Schmidt-University

University of the Federal Armed Forces, 22043 Hamburg, Germany

[c] Institute of Materials Science, Faculty of Engineering, Kiel University, 24143 Kiel, Germany

Abstract: In this research, Mg-Ca binary alloys are evaluated as anode material candidates for primary Mg-air batteries. The effect of Ca content on self-corrosion and discharge performance of Mg anode is investigated through microstructure characterization, electrochemical measurements and half-cell discharge tests. Then the composition of Mg-Ca alloys is optimized in terms of reduced self-corrosion and improved discharge performance. The basic characteristics of Mg-air batteries with optimized Mg-Ca alloy as anode are tested and compared to those based on high purity Mg and defined commercial Mg alloys. The results show that Mg-0.1wt. % Ca alloy has the best self-corrosion behavior and discharge performance among all prepared Mg-Ca alloys. The Mg-air battery with Mg-0.1wt. % Ca alloy as anode offers higher cell voltage and specific energy than those based on high purity Mg, AM50 and AZ31 alloys.

Keywords: Magnesium-calcium alloy, Magnesium-air battery, Self-corrosion, Discharge properties

1. Introduction

Metal-air batteries exhibit high specific energy density because they utilize oxygen from atmosphere as oxidant, reducing the weight of battery system [1]. Besides, the consumption of electrode materials in metal-air batteries does not cause CO_2 emissions into the environment. Hence, metal-air batteries are becoming promising power source for electric devices and vehicles. Some metals such as lithium, zinc, magnesium and aluminum are possible anode materials for metal-air batteries and have been researched

* Corresponding author.
  E-mail address: Min.Deng@hzg.de (M. Deng), Telephone number: +49 (0)4152 871936, Postal address: Helmholtz-Zentrum Geesthacht, Max-Planck-Str. 1, 21502 Geesthacht, Germany.

by many scholars in recent decades [2-5]. Among these metals, Mg attracts much attention because it has second-most negative electrode potential (i.e., -2.37 V (vs. SHE)), high theoretical specific capacity (i.e., 2.2 A h g^{-1}), high specific energy density (i.e., 6.8 kW h kg^{-1}) and relatively low cost. In principle, Mg-air batteries can be designed as primary batteries as well as rechargeable batteries. However, rechargeable Mg-air batteries are still far from being practical because of low energy conversion efficiency and low high-rate stability attributed to the absence of suitable electrolytes and efficient catalysts at air cathodes [6, 7]. In contrast, aqueous primary Mg-air battery systems can be easily assembled and reused through replacing exhausted Mg anodes. The aqueous electrolytes can be simple saline solutions that are easy to get and environmentally benign. Unfortunately, despite these advantages, the practical application of Mg-air batteries is still limited due to some technical issues [4]. Firstly, the operating voltage of Mg-air batteries is much lower than the theoretical value because of the voltage drop caused by the corrosion products on anode/electrolyte interface and sluggish kinetics of electrode reaction. Secondly, Mg suffers severe self-corrosion during discharge in aqueous electrolyte, reducing the utilization efficiency and specific energy density of anodes. This unexpected parasitic reaction leads to huge efficiency loss of Mg-air battery systems.

To solve these issues and promote the application of Mg-air batteries, developing novel Mg alloys as anode materials is a feasible method. Up to now, some Mg alloys such as Mg-Al-Zn [8, 9], Mg-Al-Mn [10], Mg-Al-Pb [11, 12], and Mg-Li [13] series alloys have been developed for Mg-air batteries, and the effect of some other alloying elements, e.g., In, Ce, Y, Sn and Ga, has been researched [11, 14, 15]. It has been reported that Mg-6 wt.% Al-5 wt.% Pb alloy shows higher discharge voltage and power density than pure Mg(99.99 wt.%) in home-made Mg-air battery test [11]. Besides, the addition of In can improve the discharge voltage of Mg-6 wt.% Al-5 wt.% Pb alloy and increase its utilization efficiency at high current densities. However, the toxic element Pb can be very harmful to the environment. According to the report of Ma et al. [13], Mg-14Li-1Al-0.1Ce alloy might be a good candidate for anodes of Mg-air batteries because of its higher operating voltage and specific capacity than pure Mg and AZ31 alloy. Nonetheless, the safety issue during the preparation of Mg-Li alloys cannot be ignored. Recently, Mg-Al-Sn alloys that are more environmentally benign attracted attention of scientists [16, 17]. Xiong et al. [17] reported that Mg-6 wt.% Al-1wt.% Sn alloys after annealing at

200 °C can exhibit similar discharge voltage and power density to Mg-Al-Pb alloy. The limiting factor of this alloy is the low utilization efficiency, which is below 50% at 10 mA cm^{-2} even after extrusion and heat treatment. Therefore, novel Mg anodes with both high discharge voltage and utilization efficiency still need to be developed.

Calcium is a fully environmentally friendly element, and it has more negative standard electrode potential than magnesium, i.e. -2.87 V (vs. SHE). Hence, it is reasonable that the addition of Ca into Mg can improve the discharge voltage of Mg anodes. It has been reported that the addition of Ca can shift the open circuit potential of Mg-Mn alloy to more negative value [18]. Yuasa et al. [19] studied the effect of Ca on the discharge performance of AM60 alloy as anode for Mg-air battery. The results show that the Ca addition can increase the specific capacity and anodic efficiency of AM60 alloy because of more uniform corrosion. Besides, owning to Ca addition, the operating time before failure of anode sheet with thickness of 1 mm increases from 11-14 hours to more than 16 hours, due to the thin and cracked discharge product layer, which allows the electrolyte to penetrate easily. Recently, research on Mg-Ca binary alloys is mainly focusing on its application as biomaterials [20-27]. As reported, Ca addition with appropriate quantity can improve the corrosion resistance of magnesium, but the measurement were mostly carried out in simulated body fluid (SBF) [24, 28].

Mg-Ca alloys might be promising candidate for anodes of primary Mg-air batteries, but there is still no systemic research on their discharge and self-corrosion properties in aqueous electrolyte for air batteries. The aim of this work is to explore the possibility of Mg-Ca binary alloys as anodes for primary Mg-air batteries. Five Mg-Ca alloys with different compositions are prepared, and their discharge and self-corrosion properties in sodium chloride solution are evaluated. At last, Mg-Ca binary alloy with optimum composition is selected and its discharge properties as anodes for lab-made Mg-air battery are compared to pure Mg and some commercial alloys.

2. Materials and methods

2.1 Materials preparation

Mg-xCa (x=0.1, 0.5, 1, 2, 4 wt.%) binary alloys were prepared via casting using pure Mg (99.96 wt. %) and pure Ca (99.0 wt. %). For comparison, pure Mg ingots were also prepared via the same

casting procedures and named as recast-Mg. The original materials were melted in a steel crucible at 760 °C with protection of Ar and SF_6 gas. Afterwards, the molten metals were poured into cylindrical steel molds with diameter of 18 mm and cooled in air. The steel molds were pre-heated at 300 °C before casting. The chemical compositions of as-cast pure Mg and Mg-Ca binary alloys were analyzed though optical emission spectrometry (spark OES) and atomic absorption spectroscopy (AAS). The results are presented in Table 1, indicating low concentrations of Fe, Ni and Cu, which are detrimental to the corrosion resistance of Mg [29-31].

Table 1 Chemical compositions of recast-Mg and Mg-Ca binary alloys (wt. %).

Materials	Ca	Fe	Al	Mn	Cu	Ni	Si	Zn	Mg
recast Mg	<0.001	0.0043	0.0054	0.0184	0.0005	<0.0002	0.0041	0.0028	Bal.
Mg-0.1Ca	0.094	0.0014	<0.01	0.032	0.0015	0.0007	0.011	0.0034	Bal.
Mg-0.5Ca	0.46	0.0013	<0.01	0.034	0.0012	0.0009	0.020	0.0033	Bal.
Mg-1Ca	1.09	0.0021	0.016	0.031	0.0011	0.0007	0.023	0.0038	Bal.
Mg-2Ca	2.25	0.0028	0.033	0.037	0.0018	0.0006	0.023	0.0032	Bal.
Mg-4Ca	3.75	0.0038	0.034	0.038	0.0019	0.0006	0.024	0.0034	Bal.

2.2 Microstructure analysis

Optical microscopy (OM) and scanning electron microscopy (SEM) were used to study the microstructure of Mg-Ca alloys. Before observation, Mg-Ca alloy samples were ground with emery papers up to 4000 grit, and then polished with oxide polishing suspension (OPS) to remove most scratches. OM images of Mg-Ca alloys were taken after etching in acetic-picric acid solution. The grain size of recast Mg and Mg-Ca alloys were measured using linear intercept method. For each material, six images of different fields of view were analyzed to measure the average grain size.

2.3 Electrochemical measurements

Potentiodynamic polarization curves were obtained by a Gamry interface 1000 potentiostat in 3.5 wt. % NaCl solution. Typical three electrodes system was used with Pt plate as a counter electrode, saturated Ag/AgCl electrode as reference and samples as working electrode. Samples were ground with emery

papers up to 1200 grit and then put into an electrochemical cell. Before testing, the samples were immersed into the solution for 30 min to get stable open circuit potential (OCP). The potentiodynamic polarization tests were proceeded within a potential range from - 400 mV to 400 mV (vs. OCP) at a scanning rate of 0.5 mV s⁻¹. Corrosion current density was calculated through extrapolating the cathodic polarization curve to corrosion potential. The region for linear fitting is between - 200 mV to - 100 mV (vs. corrosion potential). Besides, electrochemical impedance spectroscopy (EIS) measurements were also performed using the same electrochemical equipment. The frequency ranged from 100 kHz to 0.01 Hz and the sinusoidal excitation voltage applied to the cells was 10 mV rms. In order to obtain stable surface state, before measurement the samples were immersed in the electrolyte for one hour. All the electrochemical tests for every material were repeated at least three times to ensure reproducibility.

2.4 Half-cell discharge tests

Discharge curves at constant current density in half-cell arrangement were tested in 3.5 wt. % NaCl solution. The discharge potential was referred to saturated Ag/AgCl electrode. The surface area for discharge testing was 1 cm², and the applied current densities were 0.5 mA cm⁻², 2 mA cm⁻², 5 mA cm⁻² and 10 mA cm⁻². After discharge, the surface morphology of these materials was characterized by SEM. Utilization efficiencies and specific capacity of recast Mg and as-cast Mg-Ca alloys were calculated after removing corrosion products from the surface with 200 g L⁻¹ chromic acid aqueous solution. The equations used for utilization efficiency and specific capacity calculation are listed as follow [19, 32]:

$$\text{Utilization efficiency (\%)} = \frac{W_{theo}}{\Delta W} \times 100\% \tag{1}$$

$$\text{Specific capacity (mAh g}^{-1}) = \frac{I \times t}{\Delta W} \times 1000 \tag{2}$$

Where I is the discharge current (A), t is discharge time (h), ΔW (g) is the weight loss of samples during discharge process and W_{theo} (g) is the theoretical weight loss due to faradaic process. Weight loss ΔW was measured by weighing the mass of samples before and after discharge. The theoretical weight W_{theo} can be calculated through the following equation [32, 33]:

$$W_{theo} = \frac{I \times t}{F \times \Sigma(\frac{x_i \times n_i}{m_i})} \qquad (3)$$

Where F represents the Faraday constant (26.8 Ah mol^{-1}), x_i, n_i, m_i represent the mass fraction, number of exchanged electrons and atomic weight, respectively, of each element in the materials.

2.5 Magnesium-air battery tests

The discharge properties of magnesium-air battery were measured in a lab-made full cell. The optimized Mg-Ca alloy as anode was tested and compared to high purity Mg (HP Mg), commercial AM50 and AZ31 magnesium alloy. The chemical compositions of HP Mg, AM50 and AZ31 alloys used in this research are listed in Table 2. The electrolyte in Mg-air battery test was 3.5 wt. % NaCl solution. The cathode was commercial air cathode with carbon/MnO$_2$ as catalysts and Nickel mesh as the current collector. The surface areas of anodes exposed to the electrolyte are all approximately 2.5 cm^2. The discharge voltage of the cell was measured at different current densities. The average voltage during a whole discharge test was calculated and set as the cell voltage of Mg-air battery. After discharge, the specific energy based on magnesium anode was calculated through the following equation [34]:

$$\text{Specific energy (Wh kg}^{-1}) = \frac{\int_0^t U \times I \times \Delta t}{\Delta W} \qquad (4)$$

Where U is the discharge voltage (V), I is the discharge current (A), t is the discharge time (h) and ΔW (kg) is the weight loss of anode during the discharge.

Table 2 Chemical compositions of materials for comparison (wt. %).

Materials	Ca	Fe	Al	Mn	Cu	Ni	Si	Zn	Mg
HP Mg	<0.0001	0.0050	0.0030	0.0008	<0.0001	<0.0002	<0.0001	0.0035	99.98
AM50	0.0011	0.0002	4.85	0.430	0.0017	0.0005	0.0637	0.0418	94.61
AZ31	0.0011	0.0011	2.97	0.358	0.0019	0.0007	0.0309	0.732	95.90

3. Results and discussion

3.1 Microstructure of Mg-Ca alloys

Fig. 1 shows the optical images of recast Mg and as-cast Mg-Ca alloys with different Ca content. It can be seen that Ca addition causes grain refinement to magnesium, and further grain refinement can be observed with increasing Ca content. The calculated average grain sizes according to OM images are presented in Table 3, indicating that the grain size decreases with increasing Ca content. Besides, distinct dendrites appears in the microstructure of Mg-Ca alloys with high Ca content ($\geq$ 2wt. %). The formation of dendrites is due to the significant constitutional undercooling in regions near to the solid/liquid interface caused by high Ca content [23]. The constitutional undercooling is also the major driving force for nucleation, so that many nucleation sites will be activated and more crystal nucleuses will form in the constitutionally undercooled zone [35]. Therefore, the grain size is likely to be smaller. In addition, because of the low solubility of Ca in Mg, numerous Ca atoms accumulate in the regions adjacent to the solid/liquid interface, thus restricting the growth of grain due to the slow diffusion of Ca atoms [23, 24, 35]. The phase composition of as-cast Mg-Ca binary alloys has been reported in many papers [22-24], indicating a typical composition consisting of α-Mg solid solution and Mg_2Ca intermetallic as shown in the Mg-Ca phase diagram [36]. The insets in Fig. 1(b, d and f) shows the SEM images of as-cast Mg-Ca alloys. Mg-0.1Ca alloy exhibits the microstructure with only some small particles distributing in the grain interior. In contrast, for Mg-Ca alloys with high Ca content, eutectic structure composed of α-Mg and Mg_2Ca exists not only along grain boundaries but also in the interdendritic regions. Obviously, the rising Ca content also causes a significant increase of Mg_2Ca phase amount as indicated by the inserted SEM images and in other papers [21, 23, 24].

Table 3 Average grain size of recast Mg and as-cast Mg-Ca alloys.

Materials	recast Mg	Mg-0.1Ca	Mg-0.5Ca	Mg-1Ca	Mg-2Ca	Mg-4Ca
Grain size (µm)	919 ± 450	497 ± 226	245 ± 46	181 ± 37	166 ± 32	142 ± 25

3.2 Open circuit potential of Mg-Ca alloys

Fig. 2a presents the open circuit potential of recast Mg and as-cast Mg-Ca alloys in 3.5 wt. % NaCl solution. After immersion in solution, the open circuit potential of recast Mg and Mg-Ca alloys all suffer

a rapid change before reaching a stable value. The immersion time for reaching the stable state varies with the Ca content. The average value of measured OCP in last 100 seconds during the whole one-hour OCP test is set as E_{oc} and shown in Table 4. It can be found that the addition of Ca in Mg can shift the E_{oc} toward negative direction. However, the E_{oc} would increase with the rising content of Ca. Mg-0.1Ca alloy exhibits most negative open circuit potential during the last 100 seconds measurement, i.e., - 1.770 V vs. Ag/AgCl. Theoretically, calcium has more negative standard electrode potential than magnesium, so the dissolution of active Ca into Mg matrix might cause a decrease of electrode potential of pure magnesium, as shown in this work. However, the E_{oc} Mg-Ca alloys become less negative with increasing Ca content, which is probably due to the different reaction rates of cathodic hydrogen evolution. Potentiodynamic polarization curves of recast Mg and Mg-Ca alloys are presented in Fig. 2b. The cathodic branch of polarization curve is driven with hydrogen evolution reaction. Obviously, the addition of calcium element shows significant effect on the cathodic process. With the increasing content of Ca, cathodic polarization curve keeps moving to position with higher current. The cathodic current density of Mg-0.1Ca alloy at -2.0 V (vs. Ag/AgCl) is 141.9 μA, while that of Mg-1Ca alloy is 877.6 μA. This indicates that the kinetic of cathodic reaction tends to be faster with higher Ca content in magnesium. The dissolution of calcium into magnesium matrix and the slow cathodic reaction rate lead to the most negative open circuit potential of Mg-0.1Ca alloy among all researched materials in this work.

Table 4 Electrochemical parameters of recast Mg and Mg-Ca alloys.

Material	E_{OC} (V vs. Ag/AgCl)	E_{corr} (V vs. Ag/AgCl)	I_{corr} (μA cm^{-2})
Pure Mg	-1.65	-1.78	84.1 ± 15.1
Mg-0.1Ca	-1.77	-1.84	63.0 ± 19.3
Mg-0.5Ca	-1.69	-1.81	132.5 ± 11.6
Mg-1Ca	-1.64	-1.74	152.9 ± 0.6
Mg-2Ca	-1.63	-1.60	427.6 ± 45.1
Mg-4Ca	-1.61	-1.56	1062.8 ± 70.8

3.3 Self-corrosion performance of Mg-Ca alloys

Self-corrosion in electrolytes during discharge is the most important factor that decreases the utilization efficiency of magnesium batteries. Therefore, it is necessary to investigate the self-corrosion performance of magnesium anodes. Values of corrosion current density, I_{corr}, extracted from polarization curves of as-cast pure Mg and Mg-Ca alloys are summarized in Table 4. The corrosion current density tends to become higher with increasing Ca content, which indicates that the self-corrosion rate of Mg-Ca alloy in NaCl solution would increase with increasing Ca content. The self-corrosion behavior of as-cast pure Mg and Mg-Ca alloys were also investigated with EIS measurements at open circuit potential. The EIS results are shown in Fig. 3. The Nyquist plots (Fig. 3a) of recast Mg, Mg-0.1Ca and Mg-0.5Ca alloy show two large capacitive loops within the whole frequency range. The high frequency capacitive loop results from the oxide film present on the surface of alloy and the one at middle frequencies is responsible for charge transfer process. On the other hand, for Mg-Ca alloys with higher Ca content ($\geq$ 1 wt. %), the middle capacitive loop diminishes, indicating a very low polarization resistance. Instead, an inductive loop at low frequency, which might be related to the non-stationality during the measurements [37], appears in EIS spectrum of Mg-1Ca, Mg-2Ca and Mg-4Ca alloys. The equivalent circuit for all materials is presented in Fig. 3b. Film resistance (R_f) and film capacitance (CPE_f) are used to present the first capacitive loop in the equivalent circuit, while R_s represents solution resistance. The middle frequency time constant is described by charge transfer resistance (R_{ct}) and electric double layer capacitance (CPE_{dl}). Besides, the incomplete inductive loop in EIS spectrum of Mg-1Ca, Mg-2Ca and Mg-4Ca alloys is not presented in the equivalent circuit since it can be originated from the non-stationarity during acquisition of impedance spectra.

Fig. 3c shows the charge transfer resistance, R_{ct}, and total resistance, R_{total}, of recast Mg and as-cast Mg-Ca alloys after fitting EIS results with Zview software. Obviously, both R_{ct} and R_{total} increase after the addition of Ca with low concentration, but will decrease with rising content of Ca. It indicates that the addition of low content of Ca can improve the corrosion resistance of Mg in NaCl solution. However, for Mg-Ca alloys, the corrosion resistance will weaken with increasing Ca content. This is consistent with the results getting from polarization curves. Mg-Ca alloy with Ca addition of 0.1% exhibits best

corrosion resistance in 3.5 wt. % NaCl solution among all researched materials in this work. The corrosion behavior of Mg-Ca alloys has been widely studied in the past decade, suggesting that the effect of Ca on the corrosion of magnesium relates to two aspects: the grain refinement of Ca addition in Mg and the precipitation of active Mg_2Ca phase [21-23]. On one hand, it has been claimed that solid film on grain boundaries is likely to be more stable compared to the bulk surface [38, 39], while grain boundaries can also act as corrosion barriers [40, 41]. Therefore, in many cases, grain refinement can be beneficial for improving the corrosion resistance of magnesium. This is one of the reasons Mg-0.1 and Mg-0.5Ca alloys have higher corrosion resistance than recast pure Mg. Besides, it is noteworthy that Fe concentration in Mg-0.1Ca and Mg-0.5Ca alloys is lower than in recast Mg, which also contribute to their different corrosion performance, even though the Fe concentrations are all below Fe tolerance limit in as-cast Mg. On the other hand, Mg_2Ca phase has been studied and claimed to be more electrochemically active than α-Mg [21, 22, 42], leading to galvanic corrosion between Mg_2Ca phase and α-Mg matrix. The increasing Ca content introduces more Mg_2Ca phase into Mg-Ca alloys, which means more micro anode-cathode sites are formed. Hence, the increasing Ca content accelerates the galvanic corrosion in Mg-Ca alloys and consecutively decreases the corrosion resistance. For Mg-Ca alloys with high Ca content, the positive effect on corrosion resistance caused by grain refinement is probably exceeded by the negative effect caused by increasing Mg_2Ca amounts, so they exhibits low corrosion resistance in sodium chloride solution.

3.4 Discharge properties of Mg-Ca alloys

Discharge curves of recast Mg and Mg-Ca alloys at different current density are measured in 3.5 wt. % NaCl solution in a half-cell. Materials that exhibit more negative discharge potential during half-cell test can possibly supply higher voltage when serve as anodes in fully assembled batteries. Discharge results of recast Mg and Mg-Ca alloys are presented in Fig. 4. The average discharge potential during complete discharge tests are calculated and listed in Table 5. All the materials can maintain relatively stable discharge potential during the whole discharge tests at different current density. However, the value of discharge potential varies with the increasing Ca content. From Fig. 4 and Table 5, we can see that most Mg-Ca alloys have more negative discharge potential than recast Mg, even though the

discharge potential becomes less negative with increasing Ca content. Mg-0.1Ca alloy shows most negative discharge potential at all current densities, such as -1.604 V (vs. Ag/AgCl) at 0.5 mA cm^{-2} compared with -1.590 V for recast Mg.

The potential of anodes during discharge can be expressed as

$$E_{anode} = E_0 - \eta_{ct} - \eta_{diff} - iR \tag{5}$$

where E_0 is the open circuit potential, η_{ct} is the charge transfer overpotential, η_{diff} is the diffusion overpotential caused by discharge products film, i is the current on load and R is the electrolyte

Table 5 Discharge properties of recast Mg and as-cast Mg-Ca alloys.

	Current (mA cm^{-2})	recast Mg	Mg-0.1Ca	Mg-0.5Ca	Mg-1Ca	Mg-2Ca	Mg-4Ca
Discharge	0.5	-1.590	-1.604	-1.600	-1.597	-1.592	-1.582
potential	2	-1.565	-1.590	-1.576	-1.569	-1.566	-1.562
(V vs. Ag/AgCl)	5	-1.520	-1.542	-1.521	-1.520	-1.518	-1.503
	10	-1.432	-1.458	-1.442	-1.445	-1.440	-1.425
Utilization	0.5	30.9 ± 1.6	39.7 ± 1.0	38.5 ± 0.2	25.6 ± 0.4	21.1 ± 1.0	14.2 ± 0.8
efficiency	2	42.5 ± 4.7	55.5 ± 0.8	50.3 ± 4.0	46.9 ± 1.2	26.5 ± 0.2	16.9 ± 2.3
(%)	5	45.8 ± 0.1	58.2 ± 2.1	53.3 ± 2.0	49.2 ± 1.3	39.5 ± 0.6	30.4 ± 1.8
	10	49.6 ± 0.7	55.6 ± 1.1	54.3 ± 1.6	50.0 ± 1.3	42.9 ± 0.1	32.6 ± 1.3
Specific capacity	0.5	660 ± 35	886 ± 22	857 ± 5	576 ± 9	467 ± 22	311 ± 17
(mAh g^{-1})	2	948 ± 106	1238 ± 17	1156 ± 93	1042 ± 27	587 ± 5	371 ± 50
	5	1022 ± 3	1299 ± 47	1188 ± 44	1093 ± 30	876 ± 13	669 ± 40
	10	1107 ± 16	1241 ± 25	1245 ± 49	1109 ± 28	950 ± 3	716 ± 28

resistance between the reference electrode and polarized anode [43, 44]. In this work, all the materials are tested with the same cell arrangement, which means the same electrolyte resistance, so that the potential loss caused by iR drop can be considered as the same. In principle, E_0 indicates the most negative value of potential one anode can present. However, during discharge, potential loss caused by η_{ct}, η_{diff} and iR drop always exists and increases with the rising current density on load [45]. From the OCP measurement results presented in Fig. 2a, we can know that the OCP difference between Mg-0.1Ca alloy and other Mg-Ca alloys ranges from 80 mV to 160 mV. However, the difference of discharge potential at different current densities is just 4 mV to 40 mV, which is much smaller than the OCP difference. This phenomenon indicates the overpotential during discharge caused by η_{ct} and η_{diff} varies with the Ca content in Mg-Ca alloys. It is not easy to calculate or measure the η_{ct} and η_{diff} separately because of the complicated physical structure of the electrodes and the unstable surface conditions. Nevertheless, EIS has been considered as a good method to investigate the η_{ct} and η_{diff} during cell operating [44, 46]. Fig. 5 presents the EIS results of recast Mg and Mg-Ca alloys after discharge at 2 mA cm^{-2} for 2 hours. The Nyquist plots of Mg-0.1Ca and Mg-0.5Ca alloys after discharge both show a large capacitive loop in high frequency, indicating a protective film in the surface. This film will inhibit the mass diffusion process, leading to large diffusion overpotential. By contrast, for recast Mg and Mg-Ca alloys with high Ca content, the loop in high frequency shrinks sharply with increasing Ca content, indicating a film with less protection. Therefore, for recast Mg and Mg-Ca alloys, the mass diffusion through the discharge products film can be easy, so that the diffusion overpotential is most likely to be low. This statement can be proven by surface morphologies of recast Mg and Mg-Ca alloys after discharge at 2 mA cm^{-2} for 2 hours, as presented in Fig. 6(a-f). The surface of Mg-0.1Ca (Fig. 6b) and Mg-0.5Ca (Fig. 6c) are covered by dense discharge products, which prevents the penetration of solution and reactants. For Mg-Ca alloys with high Ca content, the discharge products covering the electrode surface are much more loose and porous. The solution and reactants can penetrate through the film easily, leading to low diffusion overpotential. Besides, from the Nyquist plots, we can see that the diameter of capacitive loop in middle frequency diminishes or even disappears with increasing Ca content, which means the charge transfer resistance will decrease with the increase of Ca

content. Therefore, Mg-Ca alloys with higher Ca content can exhibit higher electrochemical activity during discharge than Mg-0.1Ca and Mg-0.5Ca alloys. In other words, the charge transfer overpotential will decrease with rising Ca content in Mg-Ca alloys. Mg-0.1Ca alloy suffers large charge transfer overpotential and diffusion overpotential during discharge, but it has much more negative OCP than other materials, so that it can still present most negative discharge potential with current densities on load.

Table 5 also presents the utilization efficiency and specific capacity of recast Mg and as-cast Mg-Ca alloys. Be similar to the self-corrosion resistance, the utilization efficiency and specific capacity can be improved by the addition of Ca, but decrease with increasing Ca content in Mg-Ca alloys. Mg-0.1Ca alloy shows the highest utilization efficiency and capacity at all current densities, such as 58.2 % and 1299 mAh g^{-1} at current density of 5 mA cm^{-2}, respectively, comparing to 30.6 % and 669 mAh g^{-1} of Mg-4Ca alloy. The utilization efficiency and specific capacity of magnesium anodes are affected not only by the self-corrosion during discharge but also by the "chunk effect" induced by the detachment of some metallic particles or pieces during discharge process [11, 19, 47]. On one hand, during discharge, self-corrosion leads to mass loss of anodes and this part of mass loss cannot be utilized to supply energy for applied loads, reducing the utilization efficiency and capacity of anodes. Therefore, the best self-corrosion resistance of Mg-0.1Ca alloy is one of the reason that it exhibits highest utilization efficiency and specific capacity among all the materials. On the other hand, during discharge, some metallic particles or pieces may drop off from the surface because other metallic parts surrounding these metallic pieces have dissolved. These detached metallic parts also cannot take part in the discharge process, thus reducing the utilization efficiency and capacity of anodes. Fig. 6(g-l) also shows the surface morphologies of recast Mg and Mg-Ca alloys after discharge at 0.5 mA cm^{-2} for 16 hours and removing discharge products with chromic acid solution. Be similar to recast Mg, the surface morphology of Mg-0.1Ca alloy after discharge indicates uniform dissolution of anode surface during discharge, so the "chunk effect" on utilization efficiency is limited. It is remarkable that many pits distribute uniformly on the surface of Mg-0.5Ca alloy after discharge (Fig. 6i). These pits are left by the preferential dissolution of Mg_2Ca phase that distributes evenly in grain interior. For Mg-Ca alloys with high Ca content, the surface morphologies after discharge are different and special, as shown in

Fig. 6(j-l). Some matrix phase has been partially dissolved, while some matrix phase is still complete. The continuously Mg_2Ca eutectic enclosing interdendritic regions (as shown in the inserted SEM images in Fig. 1(d, f)) has been preferentially dissolved, leaving some narrow cracks around these matrix phase. The dissolution of eutectic continues deeply and, unavoidably, promotes the undercutting of matrix phase, leading to the detachment of some undissolved grains. This is consistent with the corrosion mechanism of Mg-Ca alloys proposed by Jeong et al [23]. Therefore, for Mg-Ca alloys with high Ca content, the "chunk effect" is severe, reducing the utilization efficiency of anodes. The detachment of undissolved grains leaves some holes on the surface of Mg-Ca alloys, as marked in Fig. 6(j-l). In addition, the detachment of undissolved grains can also be observed clearly by SEM images of Mg-4Ca alloys after discharge at 10 mA cm^{-2} for 8 hours, as shown in Fig. 7. The marked region in discharge products is confirmed to be Mg matrix pieces by the inserted EDX results. These undissolved metallic pieces have been detached from Mg anodes surface and would be dissolved independently. In conclusion, Mg-Ca alloys with low Ca content (0.1 wt. % and 0.5 wt. %) have high utilization efficiency and specific capacity because of the high self-corrosion resistance and limited impact of "chunk effect". Mg-Ca alloys with high Ca content show low self-corrosion resistance and severe "chunk effect", so that their utilization efficiencies and capacity are much lower.

3.5. Magnesium-air battery properties

In half-cell measurements, Mg-0.1Ca alloy shows best discharge potential and utilization efficiency among all Mg-Ca alloys. Therefore, we select Mg-0.1Ca alloy as the optimized Mg-Ca alloy and test its discharge properties as anode in full-assembled Mg-air battery. High purity Mg, AZ31 and AM50 alloys are also tested in the same Mg-air battery configuration for comparison. Fig. 8a shows the discharge curves of Mg-air batteries with different anodes at 0.5 mA cm^{-2}. At the initial stage of nearly half an hour, the voltage of Mg-air battery with Mg-0.1Ca anode decreases sharply, due to the accumulation of discharge products on the anode surface. Afterwards, the voltage keeps stable during the whole discharge process of more than 15 hours. Fig. 8 also presents the discharge properties of Mg-air batteries with different Mg alloy anodes at different current densities, including cell voltage (Fig. 8b) and specific energy (Fig. 8c). Mg-air battery with Mg-0.1Ca alloy as anode exhibits higher cell

voltage at all current densities than Mg-air batteries with other alloys as anode. The open circuit voltage (OCV) of Mg-air battery with Mg-0.1Ca anode can reach 2.032 V, which is higher than HP Mg (1.925 V) and also higher than that of Mg-Al-Pb anode (1.8 V) as tested by Wang et al. (3.5 wt. % NaCl as electrolyte, MnO_2 as cathode catalyst) [11]. At current density of 0.5 mA cm^{-2}, the cell voltage of Mg-air battery with Mg-0.1Ca as anode can reach 1.6 V. Besides, from Fig. 8c we can also see that Mg-0.1Ca alloy can supply higher specific energy than HP Mg and other magnesium alloys when serves as anode for Mg-air battery, especially at high current densities. The peak specific energy of Mg-0.1Ca alloy in Mg-air battery can be above 1800 Wh kg^{-1}. At current density of 10 mA cm^{-2}, its specific energy is 1429 Wh kg^{-1}, higher than that of Al anode after equal channel angular pressing (1096 Wh kg^{-1}) in Al-air system with 2 M NaCl as electrolyte as reported [48]. Accordingly, Mg-0.1Ca alloy can be a promising candidate for anode of Mg-air batteries. Besides, it is notewothy that the cell voltage and specific energy of HP Mg in Mg-air battery can be much higher than AZ31 and AM50 alloys and close to those of Mg-0.1Ca alloy. Interestingly, this situation just happens when discharging at low current densities. With increasing discharge current density, Mg-air battery with HP Mg as anode can just offer cell voltage and specific energy which are approximate to those of Mg-batteries with AZ31 and AM50 anodes, and much lower than that based on Mg-0.1Ca alloy. The reason for this phenomenon is still not clear and need to be studied further in the future.

4. Conclusions

In this work, the effect of Ca content on self-corrosion and discharge performance of magnesium is investigated. The chemical composition of Mg-Ca alloys is optimized for best half-cell discharge performance. Afterwards, the basic characteristics of Mg-air battery with optimized Mg-Ca alloy as anode are measured and compared to those based on high purity Mg (50 ppm Fe), AM50 and AZ31 alloys. As a result, the following conclusions can be drawn:

(1) The addition of Ca improves the discharge performance of magnesium, due to the high electrochemical activity of Ca and the induced grain refinement. However, with the increasing Ca content, discharge potential of Mg-Ca alloys becomes less negative and the utilization efficiency tends

to be lower because of the increasing amount of Mg_2Ca phase. Mg-0.1Ca alloy shows best discharge potential, highest utilization efficiency and capacity among all prepared alloys.

(2) Mg-air battery with Mg-0.1Ca alloy as anode shows higher cell voltage and specific energy than those based on high purity Mg, AM50 and AZ31 alloys. The open circuit voltage of Mg-air battery based on Mg-0.1Ca alloy is up to 2.0 V and the cell voltage reaches 1.6 V at current density of 0.5 mA cm^{-2}. The peak specific energy of Mg-0.1Ca anode appears at current density from 2 to 10 mA cm^{-2} and reaches above 1800 Wh kg^{-1}.

(3) Mg-Ca alloys with appropriate low Ca content (e.g., 0.1 wt. %) are the promising candidates as anode material of Mg-air batteries.

5. Acknowledgements

References

[1] Md. Rahman, X. Wang, C. Wen, Journal of The Electrochemical Society, 160 (2013) A1759-A1771.
[2] A. Kraytsberg, Y. Ein-Eli, Journal of Power Sources, 196 (2011) 886-893.
[3] Y. Li, H. Dai, Chem Soc Rev, 43 (2014) 5257-5275.
[4] T. Zhang, Z. Tao, J. Chen, Mater. Horiz., 1 (2014) 196-206.
[5] D.R. Egan, C. Ponce de León, R.J.K. Wood, R.L. Jones, K.R. Stokes, F.C. Walsh, Journal of Power Sources, 236 (2013) 293-310.
[6] C.-S. Li, Y. Sun, F. Gebert, S.-L. Chou, Advanced Energy Materials, 7 (2017) 1700869.
[7] R. Mohtadi, F. Mizuno, Beilstein J Nanotechnol, 5 (2014) 1291-1311.
[8] M. Yuasa, X. Huang, K. Suzuki, M. Mabuchi, Y. Chino, Materials Transaction, 55 (2014) 1202-1207.
[9] G. Huang, Y. Zhao, Y. Wang, H. Zhang, F. Pan, Materials Letters, 113 (2013) 46-49.
[10] Y.D. Milusheva, R.I. Boukoureshtlieva, S.M. Hristov, A.R. Kaisheva, Bulgarian Chemical Communications, 43 (2011) 42-47.
[11] N. Wang, R. Wang, C. Peng, B. Peng, Y. Feng, C. Hu, Electrochimica Acta, 149 (2014) 193-205.
[12] L.Q. Wang, R.C. Wang, Y. Feng, M. Deng, N.G. Wang, Journal of The Electrochemical Society, 164 (2017) A438-A446.
[13] Y. Ma, N. Li, D. Li, M. Zhang, X. Huang, Journal of Power Sources, 196 (2011) 2346-2350.
[14] Y. Lv, Y. Xu, D. Cao, Journal of Power Sources, 196 (2011) 8809-8814.

[15] S. Yuan, H. Lu, Z. Sun, L. Fan, X. Zhu, W. Zhang, Journal of The Electrochemical Society, 163 (2016) A1181-A1187.

[16] T. Zheng, Y. Hu, Y. Zhang, S. Yang, F. Pan, Materials & Design, 137 (2018) 245-255.

[17] H. Xiong, K. Yu, X. Yin, Y. Dai, Y. Yan, H. Zhu, Journal of Alloys and Compounds, 708 (2017) 652-661.

[18] J.G. Kim, Y.W. Kim, Materials and Corrosion, 52 (2001) 137-139.

[19] M. Yuasa, X. Huang, K. Suzuki, M. Mabuchi, Y. Chino, Journal of Power Sources, 297 (2015) 449-456.

[20] C.L. Liu, Y.J. Wang, R.C. Zeng, X.M. Zhang, W.J. Huang, P.K. Chu, Corrosion Science, 52 (2010) 3341-3347.

[21] N.T. Kirkland, N. Birbilis, J. Walker, T. Woodfield, G.J. Dias, M.P. Staiger, Journal of Biomedical Materials Research Part B: Applied Biomaterials, 95 (2010) 91-100.

[22] J.W. Seong, W.J. Kim, Acta Biomater, 11 (2015) 531-542.

[23] Y.S. Jeong, W.J. Kim, Corrosion Science, 82 (2014) 392-403.

[24] S.E. Harandi, M. Mirshahi, S. Koleini, M.H. Idris, H. Jafari, M.R.A. Kadir, Materials Research, 16 (2013) 11-18.

[25] R.-C. Zeng, W.-C. Qi, H.-Z. Cui, F. Zhang, S.-Q. Li, E.-H. Han, Corrosion Science, 96 (2015) 23-31.

[26] J. Song, Z. Wang, Y. Huang, A. Srinivasan, F. Beckmann, K.U. Kainer, N. Hort, Metallurgical and Materials Transactions A, 46 (2015) 6003-6017.

[27] M. Mohedano, B.J.C. Luthringer, B. Mingo, F. Feyerabend, R. Arrabal, P.J. Sanchez-Egido, C. Blawert, R. Willumeit-Römer, M.L. Zheludkevich, E. Matykina, Surface and Coatings Technology, 315 (2017) 454-467.

[28] Y. Wan, G. Xiong, H. Luo, F. He, Y. Huang, X. Zhou, Materials & Design, 29 (2008) 2034-2037.

[29] D. Hoche, C. Blawert, S.V. Lamaka, N. Scharnagl, C. Mendis, M.L. Zheludkevich, Phys Chem Chem Phys, 18 (2016) 1279-1291.

[30] D. Mercier, J. Swiatowska, S. Zanna, A. Seyeux, P. Marcus, Journal of The Electrochemical Society, 165 (2018) C42-C49.

[31] S.V. Lamaka, B. Vaghefinazari, D. Mei, R.P. Petrauskas, D. Höche, M.L. Zheludkevich, Corrosion Science, 128 (2017) 224-240.

[32] M.C. Lin, C.Y. Tsai, J.Y. Uan, Corrosion Science, 51 (2009) 2463-2472.

[33] Y.Y. Chen, T. Duval, U.D. Hung, J.W. Yeh, H.C. Shih, Corrosion Science, 47 (2005) 2257-2279.

[34] L. Fan, H. Lu, Journal of Power Sources, 284 (2015) 409-415.

[35] Y.C. Lee, A.K. Dahle, D.H. Stajohn, Metallurgical and Materials Transactions A, 31A (2000) 2895-2906.

[36] M. Mezbahul-Islam, A.O. Mostafa, M. Medraj, Journal of Materials, 2014 (2014) 1-33.

[37] V. Shkirskiy, A.D. King, O. Gharbi, P. Volovitch, J.R. Scully, K. Ogle, N. Birbilis, Chemphyschem, 16 (2015) 536-539.

[38] K.D. Ralston, N. Birbilis, C.H.J. Davies, Scripta Materialia, 63 (2010) 1201-1204.

[39] H.S. Kim, G.H. Kim, H. Kim, W.J. Kim, Corrosion Science, 74 (2013) 139-148.

[40] N.N. Aung, W. Zhou, Corrosion Science, 52 (2010) 589-594.

[41] T. Zhang, Z. Ji, S. Wu, Materials & Design, 32 (2011) 2742-2748.

[42] A.D. Südholz, N.T. Kirkland, R.G. Buchheit, N. Birbilis, Electrochemical and Solid State Letters, 14 (2011) C5-C7.

[43] David Linden, T.B. Reddy, Handbook of Batteries, McGraw-Hill, New York, 2002.

[44] S. Nakamura, H. Nishikawa, T. Aoki, Y. Ogami, Journal of Power Sources, 186 (2009) 278-285.

[45] C Daniel, J. Besenhard, Handbook of Battery Materials, Wiley-VCH, Weinheim, 2012.

[46] X. Yan, M. Hou, L. Sun, D. Liang, Q. Shen, H. Xu, P. Ming, B. Yi, International Journal of Hydrogen Energy, 32 (2007) 4358-4364.

[47] N. Wang, R. Wang, C. Peng, Y. Feng, Corrosion Science, 81 (2014) 85-95.

[48] L. Fan, H. Lu, J. Leng, Electrochimica Acta, 165 (2015) 22-28.

Figure Captions

Fig. 1. Optical micrographs of: (a) recast Mg; (b) Mg-0.1Ca; (c) Mg-0.5Ca; (d) Mg-1Ca; (e) Mg-2Ca; (f) Mg-4Ca. The insets in (b) (d) and (f) are corresponding SEM images.

Fig. 2. OCP (a) and polarization curves (b) of recast Mg and Mg-Ca alloys in 3.5 wt. % NaCl solution.

Fig. 3. EIS results of recast Mg and as-cast Mg-Ca alloys at OCP in 3.5 wt. % NaCl solution: (a) Nyquist plots; (b) Equivalent circuit; (c) Charge transfer resistance and total resistance after fitting.

Fig. 4. Discharge curves of recast Mg and Mg-Ca alloys in 3.5 wt. % NaCl solution at current density:(a) 0.5 mA cm^{-2}; (b) 2 mA cm^{-2}; (c) 5 mA cm^{-2}; (d) 10 mA cm^{-2}.

Fig. 5. Nyquist plots of recast Mg and Mg-Ca alloys after discharge in 3.5 wt. % NaCl solution at 2 mA cm^{-2} for 2 hours.

Fig. 6. Surface morphologies of (a) recast Mg, (b) Mg-0.1Ca, (c) Mg-0.5Ca, (d) Mg-1Ca, (e) Mg-2Ca, (f) Mg-4Ca after discharge in 3.5 wt. % NaCl solution at 2 mA cm^{-2} for 2 hours, and surface morphologies after discharge at 0.5 mA cm^{-2} for 16 hours and removing all discharge products: (g) recast Mg, (h) Mg-0.1Ca, (i) Mg-0.5Ca, (j) Mg-1Ca, (k) Mg-2Ca, (l) Mg-4Ca.

Fig. 7. SEM image of Mg-4Ca alloy after discharge in 3.5 wt. % NaCl solution at 10 mA cm^{-2} for 8 hours (cross section).

Fig. 8. Discharge properties of Mg-air batteries with different anodes: (a) discharge curves at current density of 0.5 mA cm^{-2}; (b) cell voltage at different current densities; (c) specific energy at different current densities. Electrolyte is 3.5 wt. % NaCl solution; Cathode is commercial air cathode with C/MnO$_2$ catalyst.
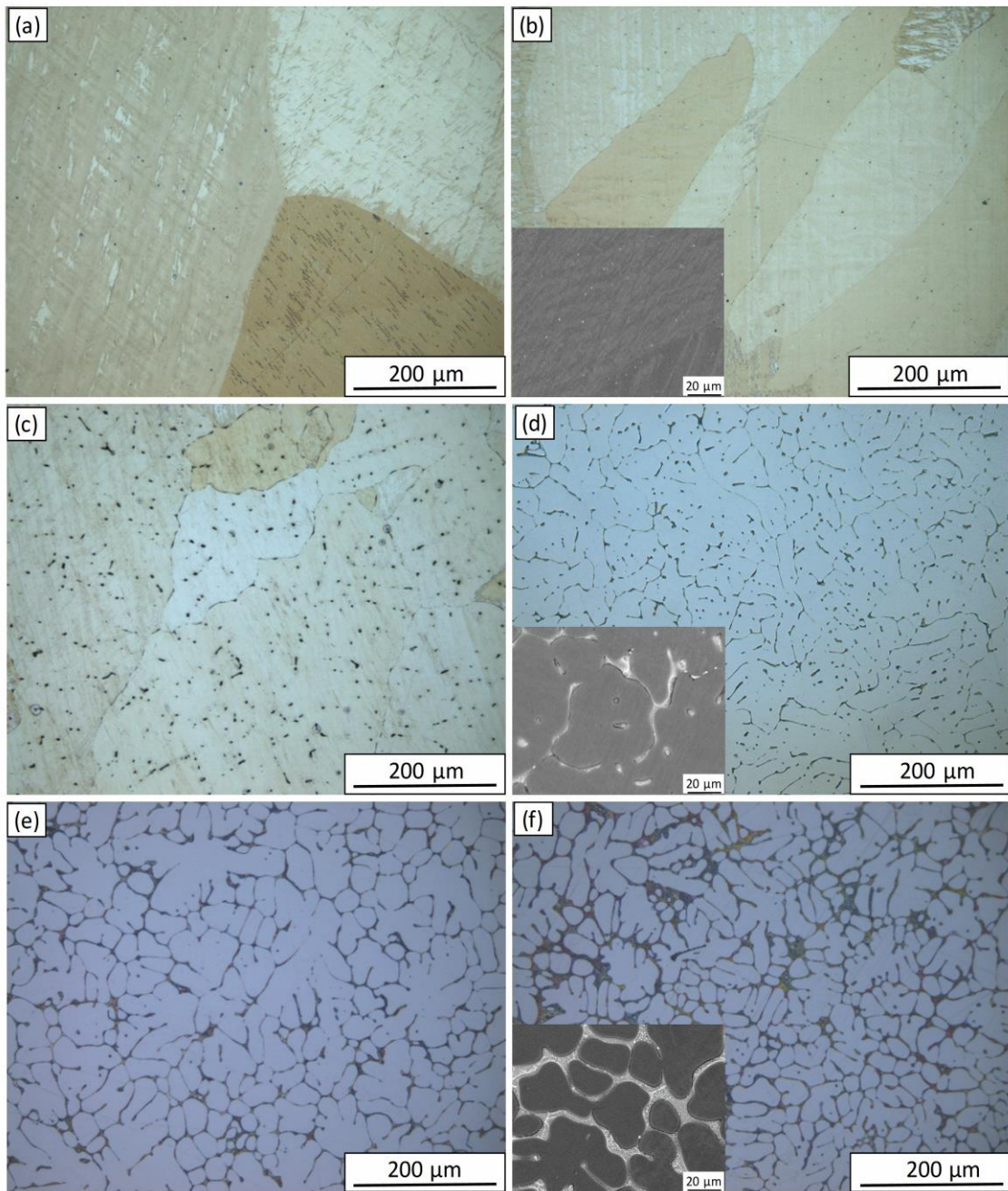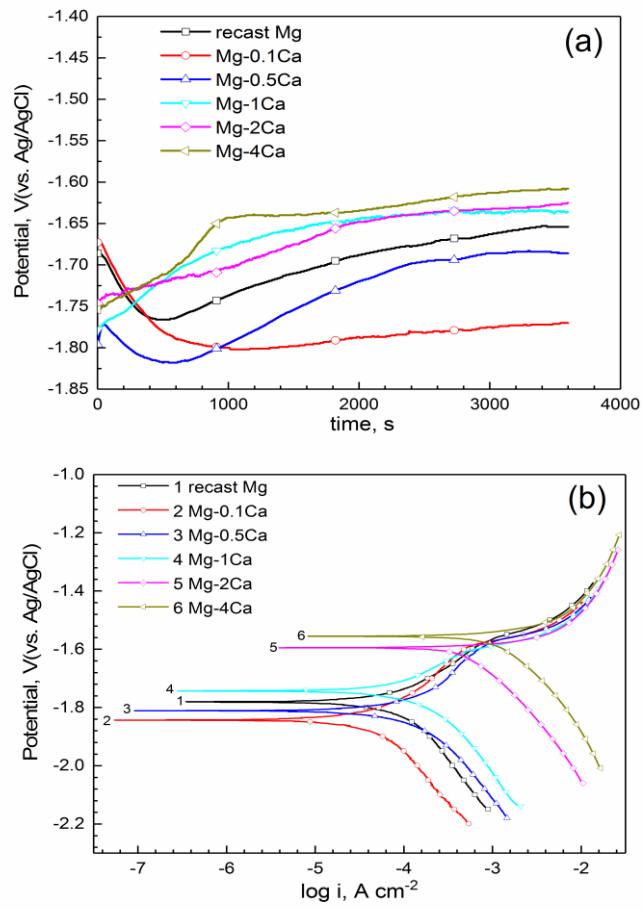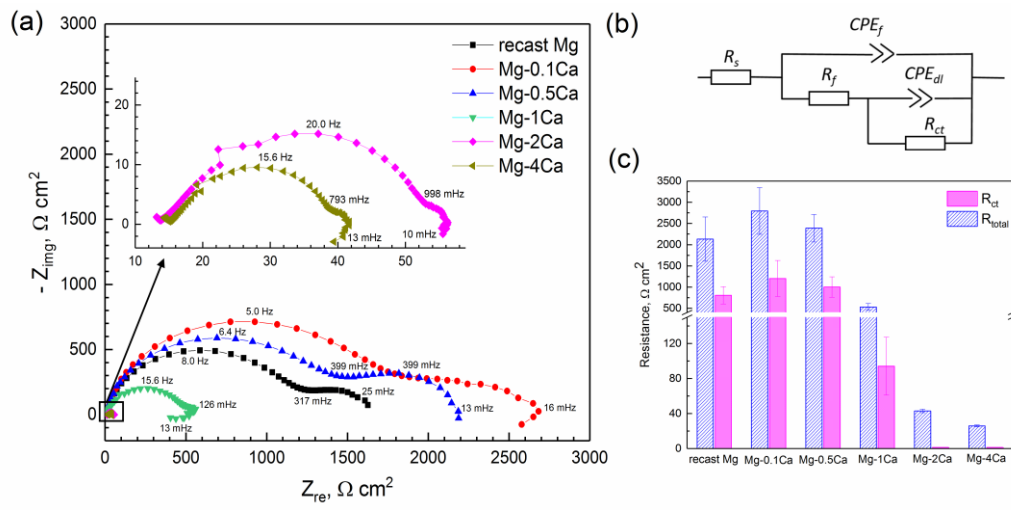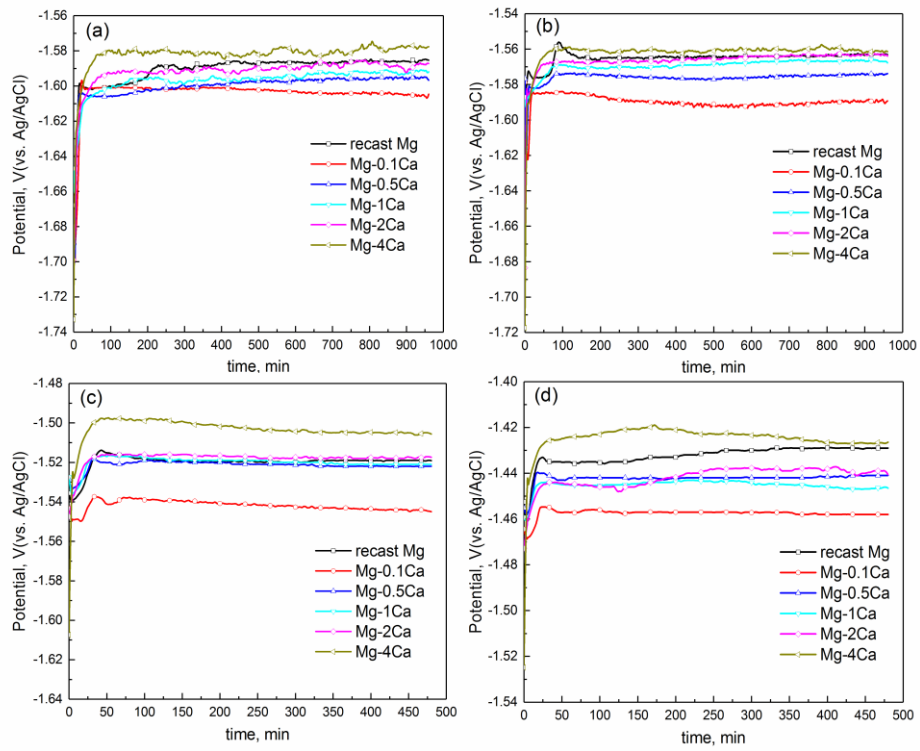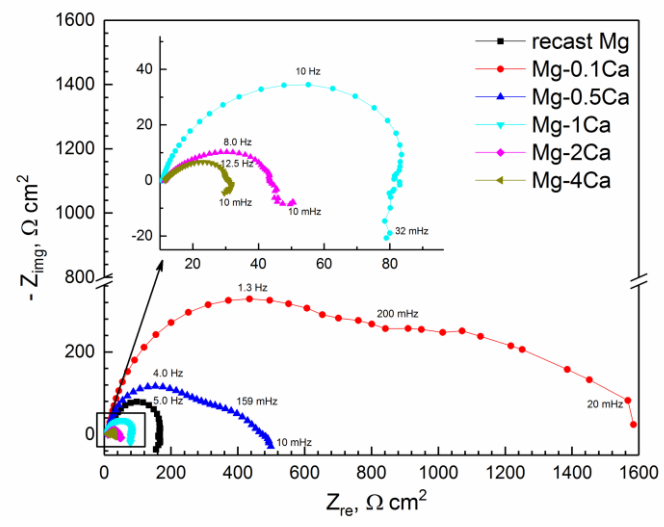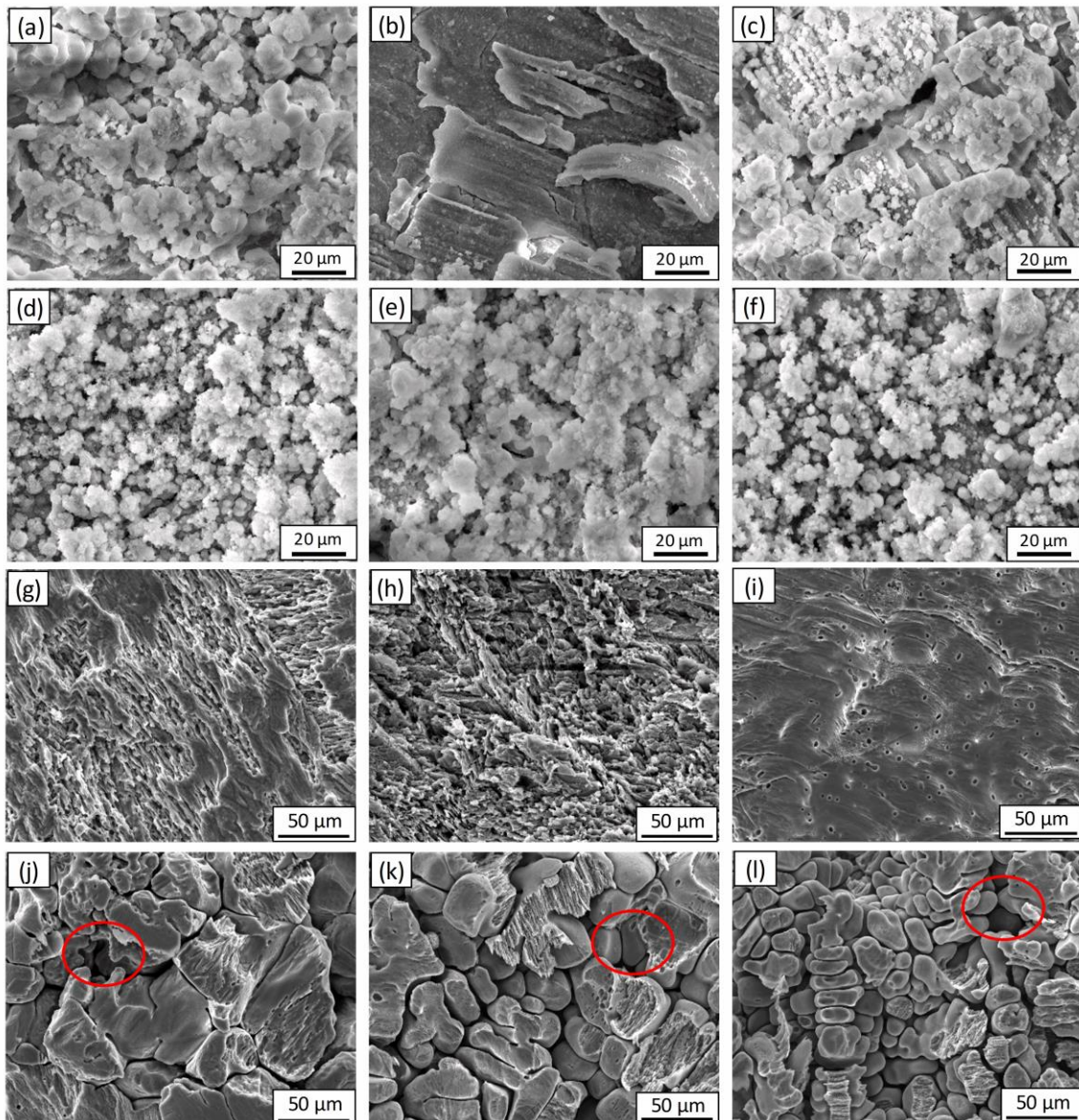
Fig. 1

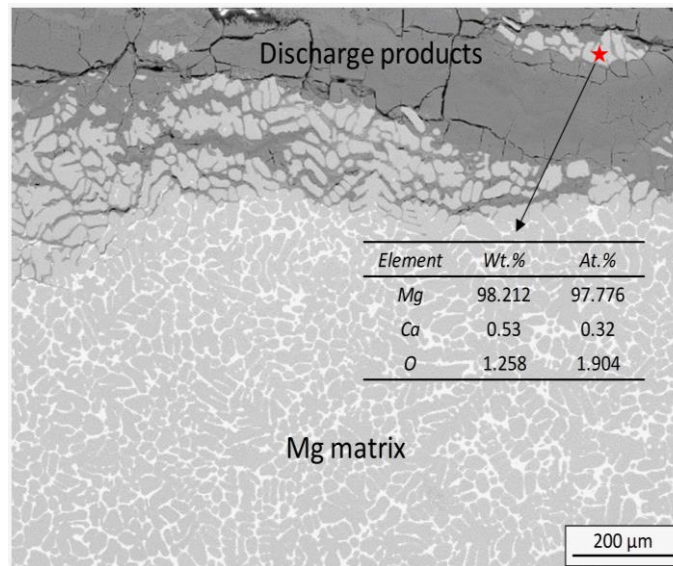**Fig. 2**

Fig. 3

Fig. 4

Fig. 5

Fig. 6

Fig. 7

Element	Wt.%	At.%
Mg	98.212	97.776
Ca	0.53	0.32
O	1.258	1.904

Fig. 8